applied sciences

MDPI

Article

Long-Term Residual Stress Monitoring via Surface Acoustic Waves Using Piezoelectric Patch Transducers

Marcel Ruetz, Mohsen Rezaei †, Maximilian Pfeiffer ‡, Sven Eck, Jürgen Maierhofer and Hans-Peter Gänser *

Materials Center Leoben Forschung GmbH, Vordernberger Straße 12, A-8700 Leoben, Austria; marcel.ruetz@mcl.at (M.R.); mohsen.rezaei@anton-paar.com (M.R.); pfeiffer.maximilian@siemens.com (M.P.); sven.eck@mcl.at (S.E.); juergen.maierhofer@mcl.at (J.M.)

* Correspondence: hp.gaenser@mcl.at

† Current address: Anton Paar GmbH, Anton-Paar-Straße 20, A-8054 Graz, Austria.

‡ Current address: Siemens Mobility Österreich GmbH, Eggenberger Straße 31, A-8020 Graz, Austria.

Abstract

Residual stresses play a crucial role in the maintenance and longevity of engineering structures. However, continuous monitoring of these stresses remains a challenge due to cost, implementation complexity, and reliability concerns. The present contribution proposes a novel method for continuous long-term residual stress monitoring by tracking the effect of residual stress changes on the propagation velocity of surface acoustic waves (SAWs) due to the acoustoelastic effect via a fixed setup of piezoelectric patch transducers (PETs). The applicability of patch transducers to stress measurement using SAW was experimentally validated using tensile and bending tests on 25CrMo4 (1.7218) steel specimens. The tensile tests exhibited a consistent decrease in wave velocity with increasing stress, enabling straightforward determination of the acoustoelastic coefficient (AEC). The bending tests confirmed the method's applicability, highlighting the need for multiple excitation frequencies to improve reliability and detect inconsistencies. Finally, it is briefly outlined how to separate residual and load stresses during long-term measurements. The results demonstrate that this approach provides a cost-effective solution for continuous monitoring of residual stresses in metallic materials, offering potential applications in structural health monitoring and predictive maintenance.

Keywords: acoustoelastic effect; residual stress; piezoelectric transducer (PET); surface acoustic wave (SAW); condition monitoring; structural health monitoring; steel

check for updates

Academic Editors: Michel Darmon and Yahui Tian

Received: 29 May 2025
Revised: 13 October 2025
Accepted: 15 October 2025
Published: 17 October 2025

Citation: Ruetz, M.; Rezaei, M.; Pfeiffer, M.; Eck, S.; Maierhofer, J.; Gänser, H.-P. Long-Term Residual Stress Monitoring via Surface Acoustic Waves Using Piezoelectric Patch Transducers. *Appl. Sci.* **2025**, *15*, 11132. https://doi.org/10.3390/app152011132

Copyright: © 2025 by the authors. Licensee MDPI, Basel, Switzerland. This article is an open access article distributed under the terms and conditions of the Creative Commons Attribution (CC BY) license (https://creativecommons.org/licenses/by/4.0/).

1. Introduction

Residual stresses are internal stresses that remain in a material after external loads are removed. They affect the fatigue lifetime markedly [1]. Most notably, compressive residual stresses introduced, e.g., by shot peening, deep rolling, or induction hardening, prevent the formation and/or growth of fatigue cracks [2]. However, it has also been observed that residual stresses relax during cyclic loading [3]. For condition-based maintenance concepts, it is therefore important to keep track of the evolution of the residual stresses during operation.

Numerous methods have been developed for residual stress measurement, including X-ray and neutron diffraction, hole-drilling, and ultrasonic techniques [4]. Despite their widespread use, many of these approaches are limited by factors such as high cost, complexity, destructiveness, or unsuitability for continuous or in situ monitoring [2,5]. These

limitations pose a significant challenge for condition-based maintenance strategies, which require long-term tracking of residual stress evolution during service.

This research employs surface acoustic waves (SAWs) to evaluate the influence of residual stresses on wave propagation via the acoustoelastic effect using piezoelectric patch transducers (PETs). By analyzing the changes in the wave velocity, the stresses can be estimated. To present this concept, the state-of-the-art monitoring methods are briefly reviewed in Section 1.1. Then, the acoustoelastic effect, which forms the foundation of the proposed system, is discussed in Section 1.2. Following this, the proposed measurement system and the test setup for experimental verification are introduced in Section 2. The experimental results obtained using the proposed system are presented in Section 3. Section 4 discusses the applicability of the method to long-term residual stress monitoring. Finally, conclusions are drawn in Section 5.

1.1. Methods of Measuring the Residual Stresses

A variety of methods exist for measuring residual stresses [2,5]. This section provides a brief review of these methods.

The first category includes mechanical methods, in which material is removed through machining, sawing, or etching to relieve residual stresses. These methods are generally destructive, but if only a small amount of material is removed, they can be classified as semi-destructive. One of the most commonly used mechanical methods is hole drilling [6]. In this method, a hole is drilled in the material's surface, causing stress relaxation and surface deformation. Strain gauges installed on the surface measure these deformations, which can then be used to calculate the residual stresses. Slitting is another similar technique, primarily used for regular geometries such as bars and beams. Instead of drilling a hole, a long slit (e.g., by sawing or electric discharge machining) is introduced into the specimen, and the resulting deformations are measured via strain gauges to estimate the residual stresses. Obviously, due to their destructive nature, these methods are not suitable for structural health monitoring.

Another major category of measurement techniques involves diffraction-based methods, which are non-destructive. X-ray diffraction (XRD) and neutron diffraction (ND) are two of the most widely used techniques. These methods are based on Bragg's law, which describes the relationship between the atomic layer spacing, the diffraction angle of the incident ray, and the wavelength of the radiation [4,6,7]. By measuring the diffraction angle and wavelength, the interlayer distances can be determined. Since residual stresses alter the atomic spacings, the stress state within the material can be estimated accurately. The typical wavelengths used in XRD range from 0.7 to 2 Å, and the penetration depth is about 25 μm, thereby measuring surface stresses [6]. ND, on the other hand, has a penetration depth of up to several centimeters in typical laboratory settings and even deeper in specialized large-scale facilities [5]. This difference arises because ND interacts with atomic nuclei, whereas XRD interacts with electrons, leading to different absorption behaviors and penetration depths.

There are also some other non-destructive and semi-destructive techniques. Magnetic Barkhausen Noise (MBN) analysis applies an abruptly varying magnetic field to a ferromagnetic sample, which causes the reorientation of the magnetic domains of the specimen. This reorientation generates electromagnetic noisy pulses, which, after signal processing, can be used to determine the stress in the material [6,8]. It is limited to ferromagnetic materials and has a stress measurement range of ±300 MPa with a penetration depth of a few millimeters.

The thermoelastic technique is based on the relationship between mechanical elastic strain and small changes in thermal energy of the elastic material [6]. By measuring these

thermal changes (in the order of 0.001 °C) using an infrared detector, the stresses can be reconstructed [9]. Due to the very small range of temperature changes, this method has a limited range and is mainly used for qualitative comparison between samples.

Optical methods such as Electronic Speckle Pattern Interferometry (ESPI) have also been applied to residual stress or defect detection. ESPI enables full-field surface deformation analysis through non-contact and non-destructive means [5]. For example, Zarate et al. demonstrated the use of out-of-plane ESPI for detecting and distinguishing cracks and fractures in aluminum plates under thermal stress [10]. Although promising, ESPI requires careful setup and is sensitive to vibrations, which can limit its practical use in industrial settings.

Digital image correlation (DIC) is another optical method that offers full-field, non-contact strain measurements that can indirectly reveal residual stress distributions. Gu et al. [11] applied DIC to assess the local mechanical behavior of welded DH36 steel, showing how strain mapping across different weld zones can indicate stress variations. While DIC is not a direct stress measurement, it is still a tool for visualizing deformation and supporting residual stress analysis.

Lu et al. [12] introduce the Dynamic Contour Method (DCM), an in-process optical approach for residual-stress estimation during laser-directed energy deposition (LDED). A fiber laser performs the build, while a CMOS camera views the track that is backlit by a separate 808 nm diode laser. Successive images are segmented to capture layer-height shrinkage; the resulting displacement field is converted to an inherent-strain load, from which the internal stress is rapidly computed.

Another method of non-destructive stress evaluation is by using ultrasonic waves and the acoustoelastic effect. Since this is the core technique employed in this research, a detailed description will be provided in the following subsection.

1.2. Acoustoelastic Effect

Hughes and Kelly [13] were among the first to experimentally investigate and theoretically describe the stress dependence of sound wave propagation in solids. Their work laid the foundation for the theory of acoustoelasticity, which is theoretically grounded in Murnaghan's theory of nonlinear elasticity [14]. According to the acoustoelastic effect, the presence of mechanical strain or stress alters the propagation velocity of ultrasonic waves in solids.

In the subsequent years, many researchers have studied stress-dependent wave propagation. Notable examples include Toupin and Bernstein [15], who described the acoustoelastic effect in perfectly elastic bodies, and Hayes and Rivlin [16], who analytically examined the propagation of plane waves under homogeneous strain fields. Crecraft [17] was the first to demonstrate the application of the acoustoelastic effect for detecting residual stresses in engineering components.

To quantify this phenomenon, the acoustoelastic coefficient (AEC) is used, characterizing the relative change in ultrasonic wave velocity due to applied stress. It is defined as follows [18]:

$$AEC = \frac{\Delta v / v_0}{\sigma} \tag{1}$$

where v_0 and V_1 denote the velocity of sound in the unstressed and stressed state, respectively, σ is the applied stress, and $\Delta v = v_1 - v_0$ represents the velocity change induced by stress.

The velocity change can be experimentally determined by measuring the difference in time of flight (ToF) between the stress-free and stressed states. This relationship is expressed as follows:

$$\frac{\Delta v}{v_0} = \frac{v_1}{v_0} - 1 = \frac{t_0}{t_1} - 1, \quad (2)$$

where t_0 and t_1 are the ToF in the stress-free and stressed states, respectively. It should be noted that due to the stress and the resulting strain, the distance between the sender and receiver will also change, making the travel distance slightly different. That effect is neglected in Equation (2), but will be discussed in more detail in Section 2.4.

The acoustoelastic method is particularly attractive for residual stress assessment due to its non-destructive nature, applicability in various geometries, and capability to provide subsurface stress information. Compared to traditional techniques, such as X-ray diffraction or hole-drilling, it enables dynamic or in-service measurements, making it suitable for real-time structural health monitoring. Despite requiring calibration and being influenced by material-specific parameters such as grain texture and temperature, its advantages in terms of depth, portability, and adaptability make it a compelling choice for the present study [18].

In the literature, several researchers have explored the use of acoustoelasticity for quantifying residual stresses. For instance, Hwang et al. [19] developed a system utilizing three wedge transducers to generate and detect longitudinal critically refracted (LCR) waves. LCR waves, also known as surface skimming longitudinal waves, can be deliberately generated in the material using specially designed wedges. These wedges are made of materials with different elastic properties and densities. More detailed information regarding the excitation and modelling of these waves can be found in [20,21]. This approach enables the evaluation of subsurface residual stresses by using the sensitivity of LCR wave velocity to stress-induced changes in the material. However, the setup requires three wedge transducers and occupies a relatively large volume, which may limit its applicability in compact or embedded systems. In contrast, the method proposed in the present study uses only two patch-type piezoelectric transducers (PETs) to generate and receive Rayleigh waves. This configuration not only reduces the system's size and complexity but also takes advantage of Rayleigh waves' strong sensitivity to surface and near-surface stress variations. As a result, the proposed method is more compact, robust, and cost-effective—making it well suited for long-term structural health monitoring applications.

In another study, acoustoelasticity was applied to evaluate residual stresses in 5052 aluminum alloy plates joined by friction stir welding (FSW) [22]. The authors used wedge transducers to generate and receive longitudinal critically refracted LCR waves, enabling the quantification of residual stresses perpendicular to the weld. Their method required calibration of the acoustoelastic coefficient for aluminum and showed good agreement with an independent stress measurement technique. In contrast, the current work focuses on steel components and utilizes surface-propagating Rayleigh waves, excited and detected by two compact PETs. This configuration eliminates the need for wedges, simplifies sensor installation, and enhances robustness for in situ structural health monitoring applications.

Xu et al. [23] proposed a simulation-based approach for reconstructing nonuniform residual stress distributions using full waveform inversion (FWI) and the adjoint method. This method directly links ultrasonic displacement to stress, enabling high-resolution stress profiling but requiring dense transducer setups and significant computational effort. In contrast, our approach uses only two PETs to generate and receive Rayleigh waves, offering a compact, experimentally validated, and practical solution for in situ residual stress monitoring.

Building on these contrasts, our work introduces a reliable and compact method for long-term monitoring of near-surface residual stresses in steel components. By permanently attaching two PETs, the system enables either continuous tracking or periodic evaluation of

residual stress relaxation during maintenance intervals. The approach combines simplicity, robustness, and repeatability, with fixed transducer placement ensuring consistent path lengths. Moreover, depending on the excitation frequency, Rayleigh waves can probe depths exceeding 1 cm—making the method well suited for structural health monitoring in real-world applications.

2. Materials and Methods

This research introduces a fixed pitch-catch setup utilizing piezoelectric patch transducers to transmit surface acoustic waves across the steel specimen surface and analyze the signals for residual stress determination. This method offers a robust, cost-effective, and continuous approach to monitoring residual stresses with sufficient accuracy.

This section presents various aspects of the implementation of the proposed measurement system.

2.1. Measurement Setup

2.1.1. Piezoelectric Transducers (PETs)

The proposed setup incorporates PETs of type P-876.SP1 from PiCeramic [24]. These transducers consist of a piezoelectric layer, connection electrodes, and an insulation layer. Their specifications are listed in Table 1. As observed, they offer a wide operating voltage and temperature range, ensuring robustness in various practical applications. Additionally, their compact size, ease of installation, and simple driver requirements make them highly suitable for industrial use. Their effectiveness has already been demonstrated in previous research [25,26]. It has to be noted that, while the much more expensive comb and electromagnetic (EMAT) transducers are specifically designed to generate surface acoustic waves (SAWs) only, the inexpensive patch transducers used in the present setup generate a mixture of various wave types. The SAW component then needs to be detected via appropriate signal processing.

Table 1. Specifications for P-876.SP1 patch transducer (data from [24]).

Property	**P-876.SP1**
Dimensions L × W × T (mm)	16 × 13 × 0.5
Minimum lateral contraction (µm/m)	650
Relative lateral contraction (µm/m/V)	1.3
Operating voltage (V)	−100 to 400
Drive type	DuraAct
Actuator type	Transducer
Piezo material	PIC255
Piezoceramic height (µm)	200
Electrical capacitance (nF)	8 (±20%)
Blocking force (N)	280
Operating temperature range (°C)	−20 to 150
Connector	Solderable contacts

2.1.2. Setup Configuration for Proof-of-Principle Tensile Experiment

As a first proof-of-principle of this inexpensive measurement system, an experiment is performed on a tensile test rig.

The experimental setup consists of a specimen made of 25CrMo4 (1.7218) steel instrumented with PETs, a sound wave generator SC600 (GAMPT GmbH, Merseburg, Germany [27]), an oscilloscope Picoscope 5444D MSO (Pico Technology Ltd., St. Neots, UK [28]), and a laptop for signal generation and recording. The GAMPT SC600 is capable of generating acoustic signals in continuous, burst, or pulse mode, with frequencies up to 20 MHz and

peak-to-peak output voltages reaching 46 V—suitable for the excitation requirements of the present study. The Picoscope 5444D offers a maximum sampling rate of 500 MS/s, corresponding to a time resolution of 2 ns, which is sufficient for capturing the fast transients of the surface acoustic waves under investigation.

The specimen measures 205 mm in length, 50 mm in width, and 5 mm in thickness. The sensors are glued with cyanoacrylate adhesive to the surface of the specimen with a spacing of 60 mm between them. The specimen is mounted inside a tensile test rig to apply the required stress.

The general configuration of the measurement system is illustrated in Figure 1a, which also demonstrates how the specimen elongates under tensile stress. A photograph of the specimen inside the tensile test rig is presented in Figure 1b, where the attached sender and receiver PETs on the specimen are clearly visible.

The results of the tests conducted on this platform are presented in Section 3.2.

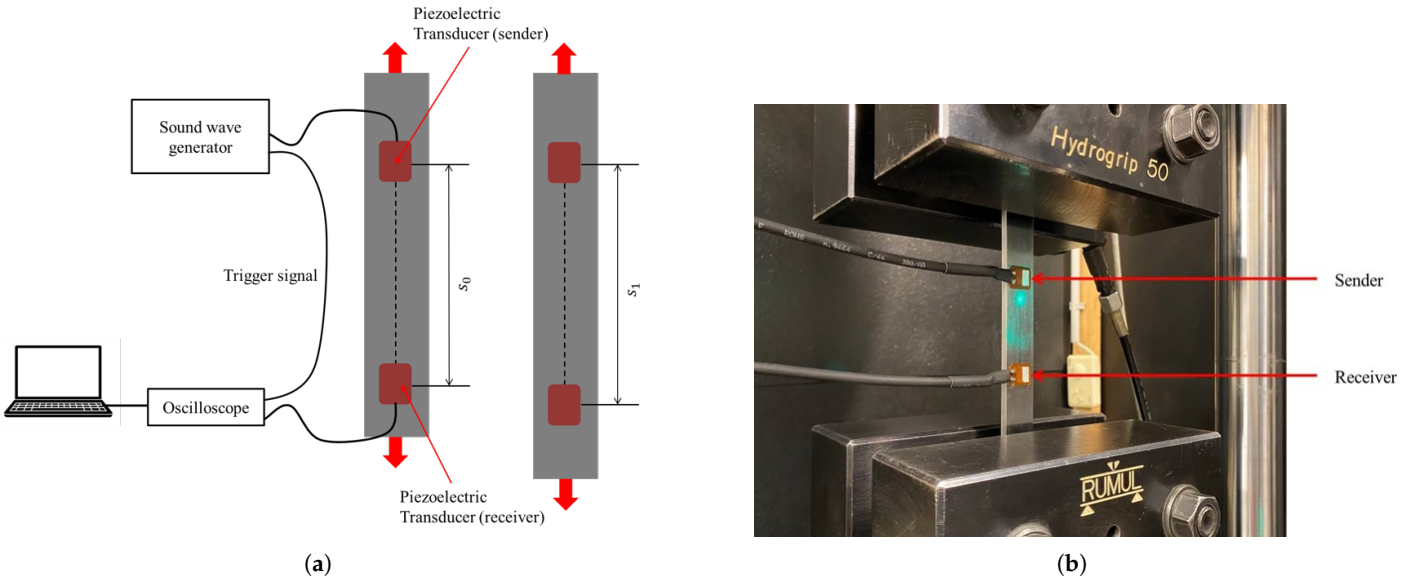


Figure 1. Proof -of-principle setup: (**a**) Measurement setup configuration. (**b**) Test rig photograph.

2.1.3. Setup Configuration for Bending Experiment

The previous setup generates a uniform tensile stress inside the material. However, it is also important to investigate the typical case in which a component undergoes bending, resulting in a stress gradient across its thickness. To achieve this, a four-point bending test setup was designed and implemented. The setup configuration is shown in Figure 2a.

When the specimen is bent under the pressure of the bending points, the lower side experiences tensile stress, while the upper side undergoes compressive stress. In the configuration shown in Figure 2a, the PETs are positioned on the lower side, thereby measuring tensile stress. Conversely, if the specimen is flipped with the PETs on the upper side, they measure compressive stress, as illustrated in Figure 2b.

The stress distribution along the specimen and across its thickness is illustrated in Figures 2c and 2d, respectively. As seen in Figure 2c, the middle supports are positioned so that the Rayleigh wave propagates along a path of constant stress between the PETs.

The results of the tests conducted on this platform will be presented in Section 3.3.

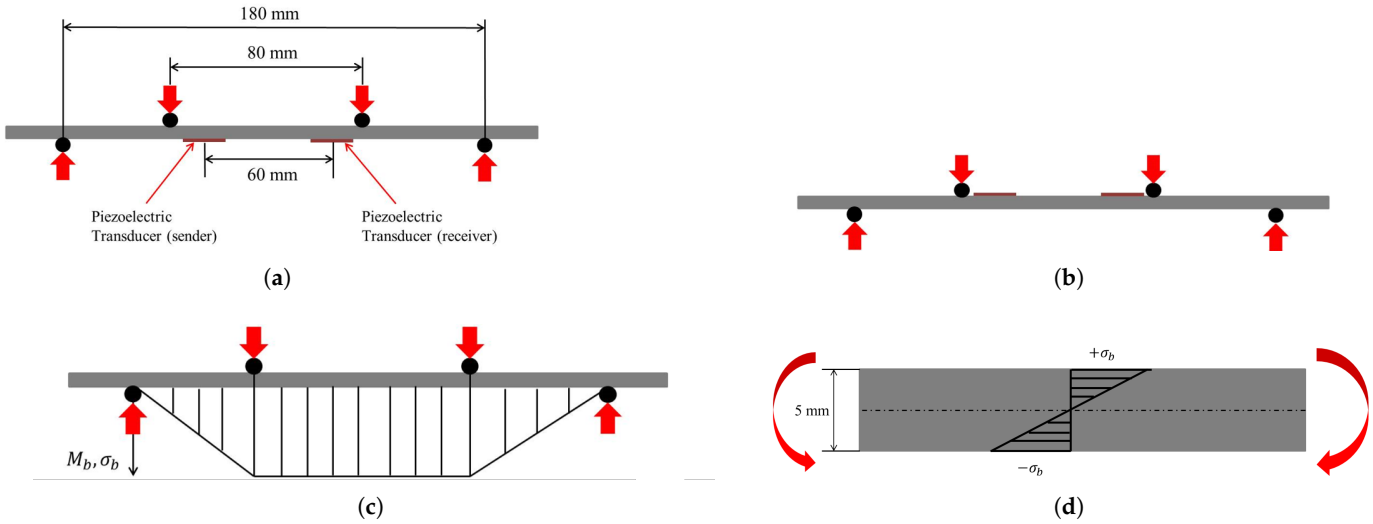


Figure 2. Four-point bending setup: (**a**) PETs positioned at the bottom, measuring maximum tensile stress. (**b**) PETs positioned at the top, measuring maximum compressive stress. (**c**) Stress distribution in the specimen under bending. (**d**) Stress profile across the specimen thickness.

The photos of the real bending setup in tensile and compressive testing modes are shown in Figures 3a and 3b, respectively. The relative positions of the PETs and supports are also clearly visible.

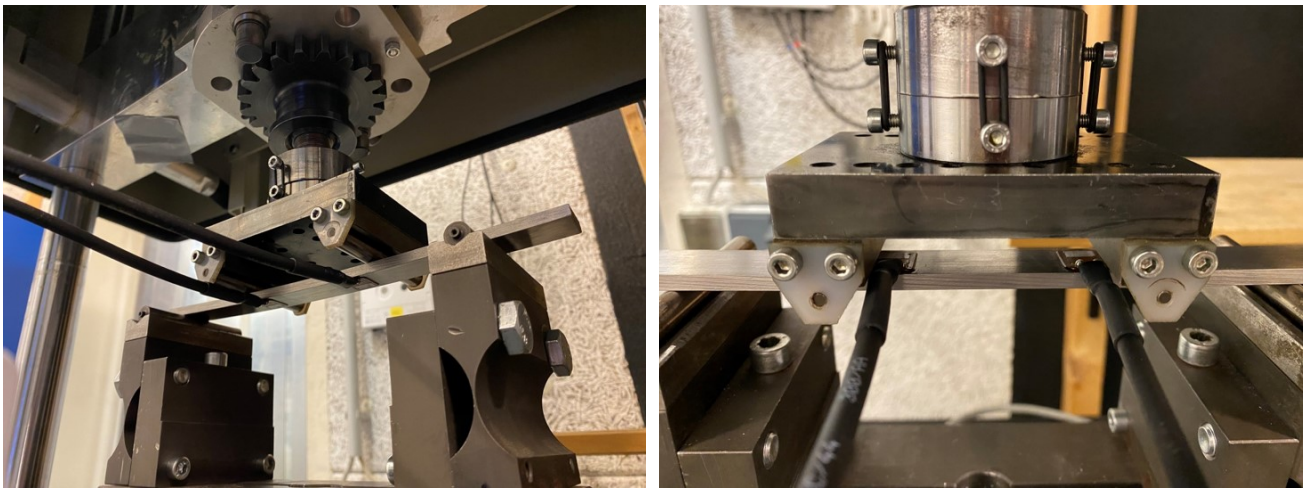


Figure 3. Photographs of the bending setup: (**a**) Tensile measurement configuration. (**b**) Compressive measurement configuration.

2.2. Signal Generation and Analysis

To excite the PETs, a series of tests were performed with varying signal lengths and frequencies in order to optimize the signal detection performance in the experimental setup.

2.2.1. Selection of Excitation Frequency

Initially, the influence of the excitation frequency on the system response was investigated. It was observed that, due to the characteristics of the measurement setup and the specimen geometry, certain frequencies yielded significantly stronger responses than others. This behavior is illustrated in Figure 4, which shows the received signals for a range of excitation frequencies.

As shown, the amplitude of the received signal increases from 1 MHz to 2 MHz and subsequently decreases with increasing frequency. For frequencies below 1 MHz, the received amplitude is low due to the damping effects of the material. Similarly, for excitation frequencies above 3 MHz, the received signal becomes negligible. This behavior is likely due to higher scattering of the signal and the limited ability of the specimen to respond to high-frequency excitation; that is, at higher frequencies, the rapid changes in the excitation waveform cannot be effectively followed by the structure.

From these observations, it is evident that an excitation frequency of 2 MHz yields the highest signal amplitude and was therefore selected for subsequent experiments.

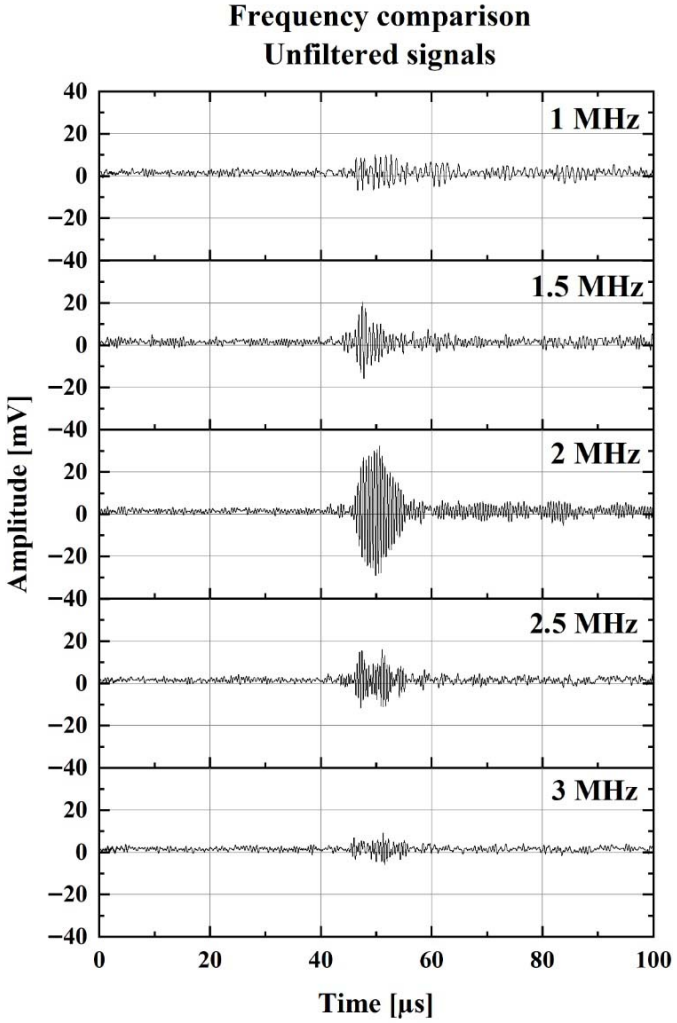


Figure 4. Received signals for various frequencies in the measurement setups.

2.2.2. Setting the Signal Length

In addition to excitation frequency, the duration of the burst signal significantly influences the quality of the received signal. To investigate this effect, three excitation signal configurations were tested on the specimen: (1) a single pulse signal with a duration of 1 µs; (2) a 1 MHz short burst signal with a total duration of 1 µs; and (3) a 2 MHz burst signal with a longer duration of 5 µs. The excitation and received signals, along with the corresponding fast Fourier transforms (FFT) of the received signals, are presented in Figure 5.

For the first two cases—namely, the single pulse and the short 1 MHz burst—the received signal appears as a compact wave packet with a clearly identifiable peak location. In contrast, the 2 MHz burst with a longer duration produces a more extended waveform,

in which identifying a distinct peak becomes more challenging. Despite this, longer signals offer several advantages that make them preferable for the current experimental setup.

First, a longer burst signal carries more energy compared to a shorter pulse of equal amplitude. This increased energy can more effectively excite the specimen, especially given the mechanical inertia and transient response time of the structure. Shorter pulses may fail to deliver sufficient energy to induce a detectable ultrasonic response.

Second, from a frequency-domain perspective, shorter time-domain signals inherently possess a broader spectral bandwidth. As a result, the received signal includes a wide range of frequency components, not all of which are relevant to the targeted excitation frequency. This effect is clearly visible in the FFT plots. While the 2 MHz burst shows a sharp spectral peak centered at 2 MHz, the other two signals exhibit a more dispersed frequency spectrum, making the dominant frequency less distinguishable.

In practical applications where signals are contaminated by measurement noise, a narrowband signal is easier to filter and isolate. A well-defined spectral peak, such as that observed in the 2 MHz burst case, facilitates the use of bandpass filtering to extract the desired signal component. In contrast, a broadband signal complicates the filtering process and increases the risk of losing useful information or retaining noise.

In summary, although shorter signals provide sharper time-domain peaks, longer burst signals with more concentrated frequency content are advantageous in noisy environments and for reliable energy transfer to the specimen. Therefore, the 2 MHz, 5 µs burst configuration is considered optimal for subsequent measurements.

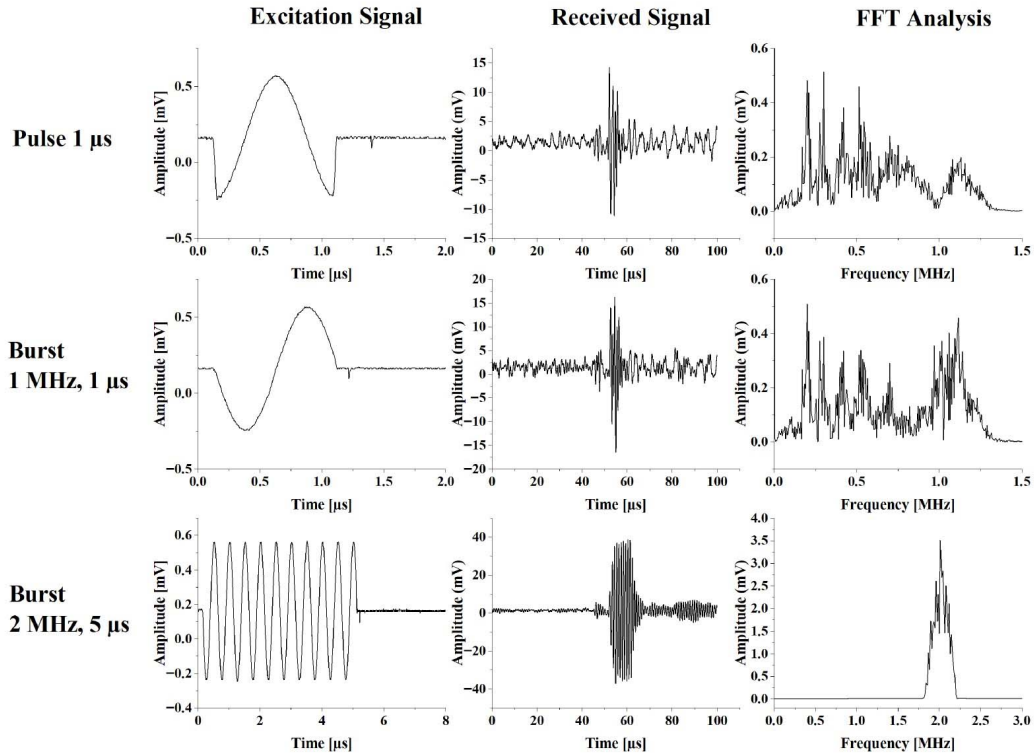


Figure 5. Excitation signals, corresponding received signals, and FFT of the received signals for various signal lengths and excitation frequencies.

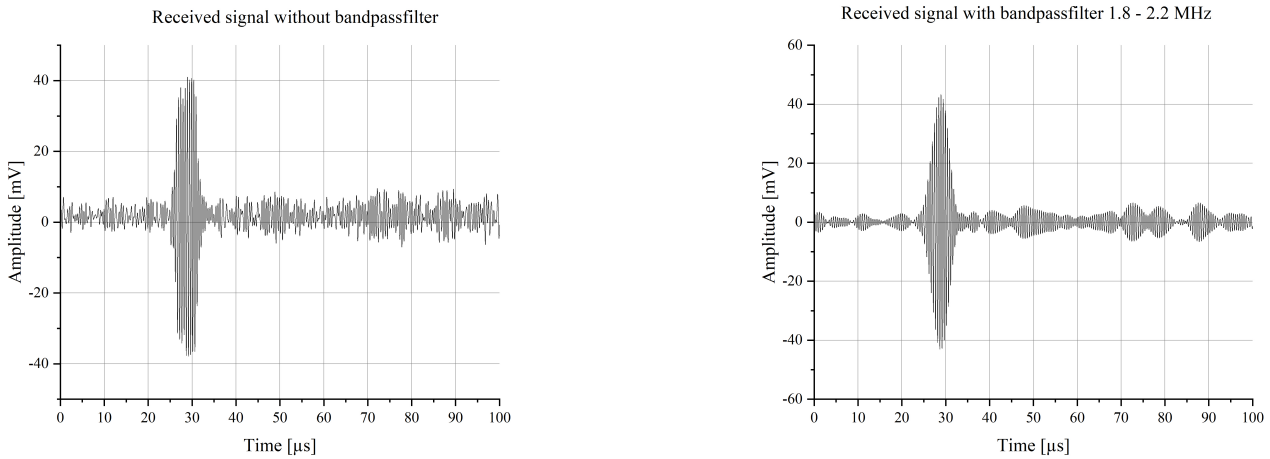
2.2.3. Filtering the Signals

As discussed in the previous subsection, both mechanical vibrations and electronic interference introduce noise into the measurement signals. To enhance signal quality and improve the reliability of time-of-flight (ToF) detection, it is necessary to apply signal

filtering. A band-pass filter (BPF) was implemented to remove frequency components outside the region of interest, thereby isolating the excitation frequency.

In the proposed setup, the BPF is centered at the excitation frequency (2 MHz) with a cutoff range of ±0.2 MHz. As seen from the FFT of the 2 MHz signal in Figure 5, this narrow bandwidth preserves the fundamental component of the excitation while effectively attenuating out-of-band noise. This approach ensures that the dominant frequency remains intact while reducing interference from other spectral components, thereby improving the accuracy and robustness of the time-of-flight (ToF) measurements.

The impact of applying the BPF to a sample 2 MHz signal is shown in Figure 6. In the unfiltered signal (Figure 6a), the presence of broadband noise obscures the main wave packet, making peak identification challenging. After filtering (Figure 6b), the noise is significantly reduced, and the dominant peak becomes clearly identifiable, facilitating accurate ToF measurement.



(**a**) (**b**)

Figure 6. Application of a band-pass filter to clean up the signals: (**a**) A sample raw received signal generated by a 2 MHz burst via the sender PET. (**b**) The same signal after band-pass filtering with lower and upper cut-off frequencies of 1.8 and 2.2 MHz, respectively.

Considering the above discussions, a 2 MHz burst signal with a duration of 5 µs was selected as the excitation signal, and a band-pass filter with cutoff frequencies of 1.8–2.2 MHz was applied to enhance the quality of the received signal.

2.3. Reference SAW Velocity and Time Offset Calculation

Another critical aspect of the analysis is measuring the SAW velocity in the stress-free specimen. This velocity serves as a reference to calculate velocity deviations due to the applied stress, thereby determining the acoustoelastic coefficient (AEC) as described in Equations (1) and (2). Additionally, to locate the approximate time-of-flight (*ToF*) of the signal for peak detection, it is essential to determine the base SAW velocity.

Apart from the velocity, the measured *ToF* also includes an offset time due to factors such as measurement delays, PET response time, and other system latencies, as described in the following equation:

$$ToF = \frac{s}{v_0} + t_{\text{offset}} \tag{3}$$

where s is the distance between the sensors.

Therefore, it is crucial to calculate this offset to determine the true SAW velocity.

To determine the stress-free SAW velocity and the system's time offset, a setup was assembled consisting of a signal generator, an oscilloscope, a PET mounted on the specimen as the excitation source, and a laser vibrometer (LVM) for signal detection, as shown in Figure 7a. The height of the LVM was finely adjustable, enabling precise measurement of the time of flight (ToF) at multiple positions along the specimen surface. Measurements were performed at distances ranging from 1 to 8 cm from the PET. The filtered received signals are shown in Figure 7b, where the detected peak positions indicate an increasing ToF trend with distance. These ToF values are plotted in Figure 7c, confirming a linear relationship, which indicates a constant SAW velocity. A linear fit yields a slope with units of time per distance, whose inverse corresponds to the SAW velocity. Based on the fit, the wave velocity was calculated as $v_0 = 3004.7$ m/s, and the y-intercept gives a system time offset of $t_{\text{offset}} = 18.75$ µs.

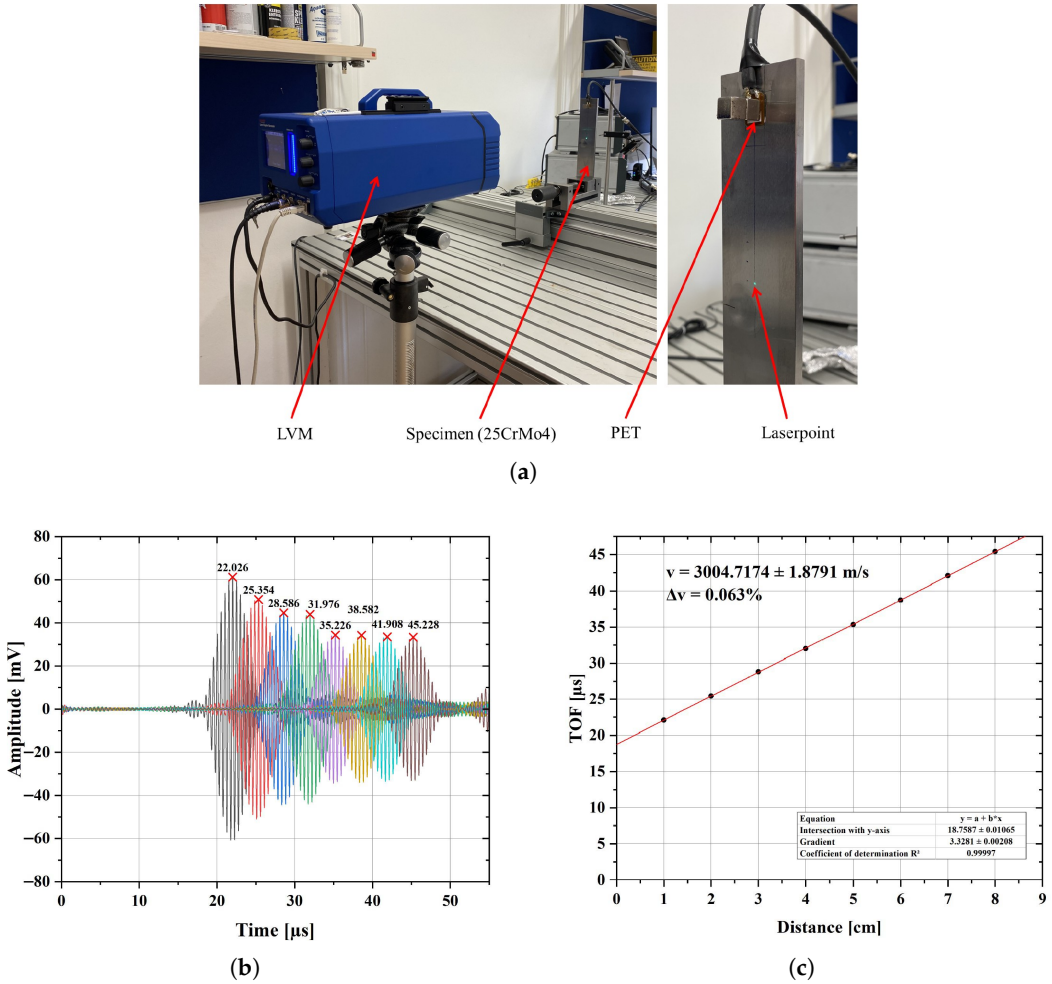


Figure 7. Measurement of sound velocity and time offset in the 25CrMo4 (1.7218) steel specimen: (**a**) experimental setup for time-of-flight (ToF) measurements; (**b**) filtered received signals at various distances, with the highest peak indicating the ToF; (**c**) and measured ToF values versus distance and the corresponding linear fit used to estimate sound velocity and system time offset.

It is worth noting that the PET-LVM configuration was used exclusively for measuring the SAW velocity, owing to the LVM's flexibility in adjusting the detection point along the specimen—an option not available in the fixed PET-PET configuration. The actual monitoring method employed in this work, as detailed in Sections 3.2 and 3.3, relies on a PET-PET arrangement. This setup offers distinct advantages for continuous structural monitoring, including compactness, robustness, and cost-effectiveness, as previously discussed.

2.4. Strain Compensation

As mentioned in Section 1.2, the elongation of the specimen due to strain is not accounted for in the initial calculations. In reality, when stress is applied, the distance between the PETs changes due to strain, thereby affecting the ToF. To obtain accurate ToF measurements, it is therefore necessary to update the equations accordingly. If the material's strain is represented by ε, the strained distance can be expressed as follows:

$$s_1 = s_0(1 + \varepsilon) \tag{4}$$

In our test rig, the applied axial force F is controlled and recorded. Given the known cross-sectional area A of the specimen, the axial stress σ is computed as follows:

$$\sigma = \frac{F}{A} \tag{5}$$

Assuming linear elastic behavior, the axial strain is then determined via Hooke's law, written as follows:

$$\varepsilon = \frac{\sigma}{E} \tag{6}$$

where E is the Young's modulus of the material.

The corresponding velocities can then be computed as follows:

$$v_0 = \frac{s_0}{t_0} \tag{7}$$

$$v_1 = \frac{s_1}{t_1} = \frac{s_0(1 + \varepsilon)}{t_1} \tag{8}$$

Thus, the relative velocity change is given by the following:

$$\frac{\Delta v}{v_0} = \frac{v_1 - v_0}{v_0} = \frac{t_0(1 + \varepsilon)}{t_1} - 1 \tag{9}$$

This implies that a correction factor of $(1 + \varepsilon)$ on the time of flight (as compared to Equation (2)) should be incorporated into the calculations to ensure accuracy.

2.5. Measurement Procedure

To consolidate the methodology, the experimental steps are summarized in the flowchart shown in Figure 8.

The process begins with mounting the specimen in the test rig, followed by exciting the sender using the selected excitation signal, viz., a 2 MHz sinusoidal wave with a duration of 5 µs. The corresponding response is recorded at the receiver.

The recorded signal is then passed through a band-pass filter to suppress noise and unwanted frequency components, yielding a cleaner signal suitable for feature extraction. The time of flight (ToF) is subsequently estimated using generalized cross-correlation with phase transform (GCC-PHAT); the correlation is evaluated only within an a priori expected time window, as illustrated in Figure 7b.

Once the current ToF (t_1) is determined, it is compared with the no-load ToF (t_0) to compute the velocity ratio using Equation (9). The calculated results are stored and visualized for further analysis.

Subsequently, the applied force is increased in defined increments, as detailed in the respective sections of the results. This measurement cycle is repeated until the target maximum force is reached. To improve reliability, each measurement can be repeated multiple times, with averaged values reported, as discussed in the Section 3.

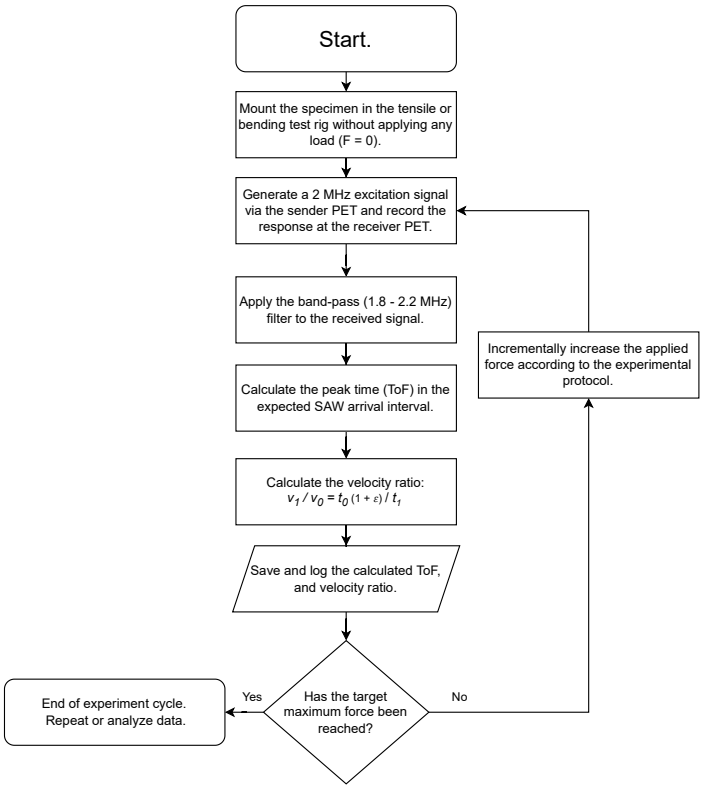


Figure 8. Flowchart illustrating the experimental procedure.

2.6. Distinction Between the Individual Wave Modes

At material interfaces, wave reflections and mode conversions occur. These phenomena—together with interference—complicate the accurate determination of the true propagation velocity. To ensure that the signals identified in the analysis are indeed Rayleigh surface waves, we first performed numerical simulations under idealized conditions, i.e., without real-world perturbations such as piezoelectric transducer inertia, noise sources, and coupling effects. The simulated specimen geometry matched that of the actual sample.

The numerical simulations were carried out with Abaqus/Explicit. Virtual sensors were defined on the model to record the elastic wavefields. The material behavior was implemented via a VUMAT user subroutine. Second- and third-order elastic constants were taken from the literature and are not listed here, as the simulations serve solely to optimize the signal-processing procedure. The initiation of elastic waves is achieved by applying a time-dependent pressure to a small area of the surface. The temporal variation of the pressure is controlled via a VDLOAD subroutine. For the analysis, we employed cross-correlation of the waveforms recorded at two sensor positions. To determine the Rayleigh wave velocity, a time window was defined around the expected inter-sensor delay of the Rayleigh wave arrival; within this window, the dominant local maximum was assigned to the Rayleigh mode. Owing to the acoustoelastic effect, this peak shifts; the window must therefore be wide enough to capture the shift, yet narrow enough to avoid ambiguity from multiple competing peaks.

The time history of the pressure signal follows the function given in Equation (10) and is illustrated in Figure 9.

$$p(t) = p_0 \exp\left(-\left(2\frac{t - t_0}{1.4t_0}\right)^2\right) \sin(2\pi f t) \tag{10}$$

where $p(t)$ denotes the time-varying pressure, p_0 is the pressure amplitude, t represents time, t_0 is the reference time, and f is the signal frequency.

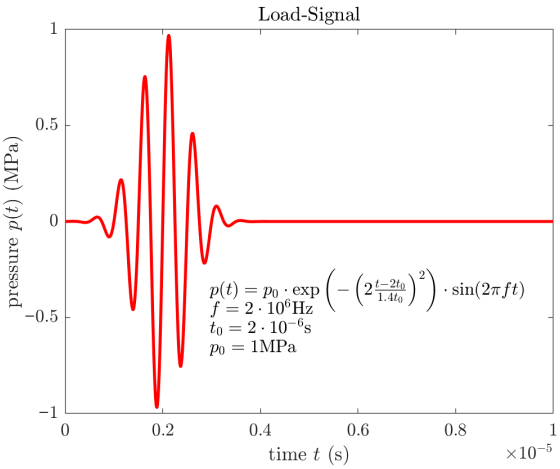


Figure 9. Representation of the time-dependent pressure signal employed to generate the elastic waves within the simulation model.

To separate the wave modes, the two sensor traces are first band-pass filtered around the excitation band and trimmed to identical length. Using the material parameters E (Young's modulus), ν (Poisson's ratio), and ρ (mass density), the target phase velocities for isotropic steel are computed for the longitudinal, shear, and Rayleigh modes, i.e., v_P, v_S, and $v_R \approx 0.9\, v_S$. These velocities are converted into expected arrival times $t_{\text{exp}} = d/v$ for each mode (with sensor spacing d), and narrow time windows are placed around each t_{exp}. Within every window, the inter-sensor delay Δt is estimated by the Generalized Cross-Correlation with Phase Transform (*GCC–PHAT*) applied to the two band-limited signals; the peak whose delay is closest to t_{exp} is selected. The corresponding apparent velocity $v_{\text{app}} = d/|\Delta t|$ is then compared against the targets $\{v_P, v_S, v_R\}$, and the mode label is assigned to the one with the smallest relative deviation. The assignment is further corroborated in the frequency domain by evaluating the cross spectrum of the two sensors: from the unwrapped inter-sensor phase, one obtains the wavenumber $k(f)$ and the frequency-dependent phase velocity $v_\phi(f) = 2\pi f/k(f)$; coherent plateaus of $v_\phi(f)$ near v_P, v_S, or v_R confirm the classification. This procedure robustly separates Rayleigh, longitudinal, and shear contributions using only the two synchronized sensor recordings. More detailed information on this methodology can be found in the following references [29–31].

3. Results

As described in Sections 2.1.2 and 2.1.3, two setups (tension and bending) were designed and implemented for this research. The results of the experiments in these setups are presented in the following subsections. As concluded in Section 2.2, a 2 MHz burst signal with a duration of 5 µs will be used in the following experiments.

3.1. Results of the Finite Element Simulations

Finite element simulations are conducted to develop an evaluation routine for specifically separating the individual wave modes from the detected data. The sample geometry and signal shape are selected to be identical to those used in the experimental test. Typical values for steel are used as material parameters. Two virtual sensors are placed at a defined distance on the numerical model in order to measure the elastic wave. Figure 10 shows the signals at the two sensor positions, whereas Figure 11 shows the determination of the temporal shift of the Rayleigh wave using cross-correlation.

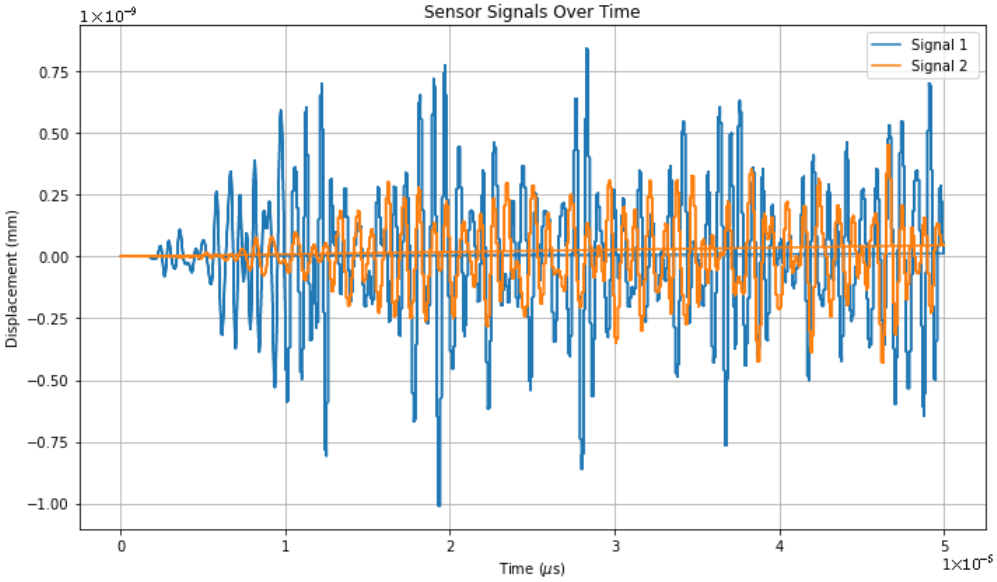


Figure 10. Simulation results: signals at the two sensor positions.

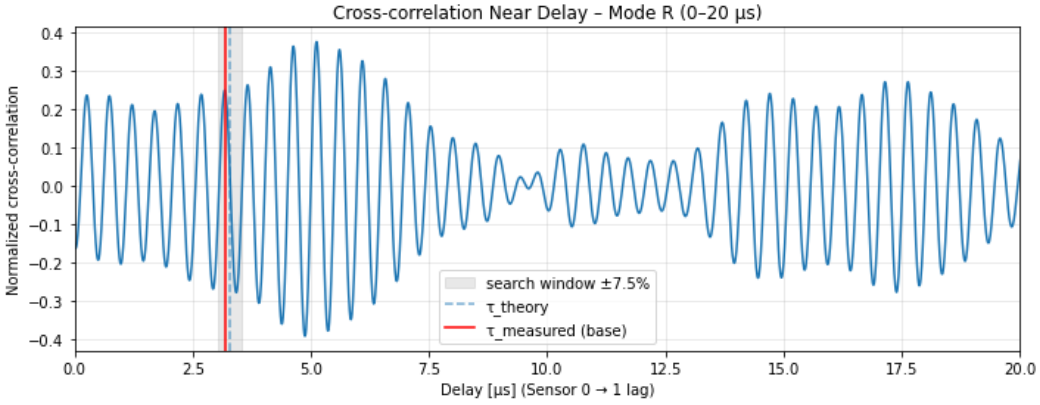


Figure 11. Cross-correlation of the simulated wave propagation with the theoretical Rayleigh wave velocity, the tolerance window and the detected peak.

3.2. Results of the Proof-of-Principle Experiment

For the proof-of-principle experiment in the tensile test rig, described in Section 2.1.2, a range of forces from 10 to 40 kN (in steps of 10 kN) was applied to the specimen, resulting in tensile stresses ranging from 100 to 400 MPa. For each force step, ten measurements were performed, and the average of the results was taken to reduce the effect of noise and uncertainties.

The results of the analysis are plotted in Figure 12. It shows the relative velocity versus applied stress for both corrected (red) and uncorrected (green) values. At every stress level the symbol marks the mean of the ten individual measurements, while the vertical error bar (caps at the bar ends) represents the standard deviation. The very small error bars demonstrate the excellent repeatability of the patch-transducer arrangement.

The results indicate that the velocity decreases as the tensile stress increases, as expected by the acoustoelastic behavior. The experiment serves as a robust proof-of-principle demonstrating that stress measurements are feasible using this inexpensive patch transducer setup. The slope of a regression line through the origin (excluding the outlier) represents the acoustoelastic coefficient (AEC), which was calculated as -15.53×10^{-6} MPa^{-1} with a standard deviation of 6.395×10^{-7} for the corrected line.

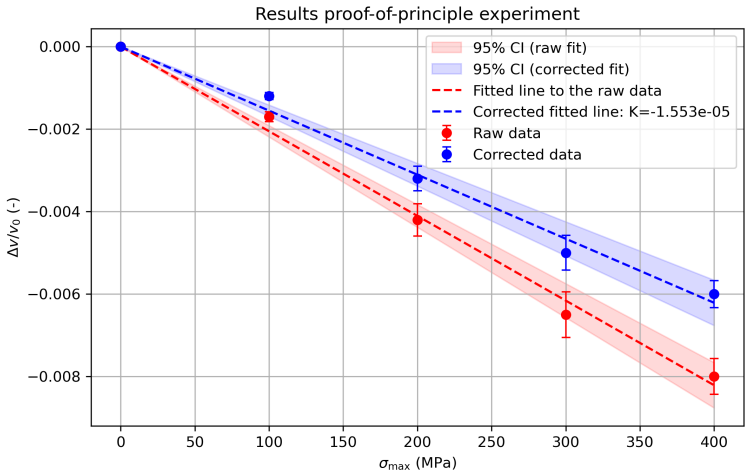


Figure 12. Results of the proof-of-principle experiment. Velocity changes due to the applied tensile stress (red: uncorrected, blue: corrected for distance changes due to the resulting stress).

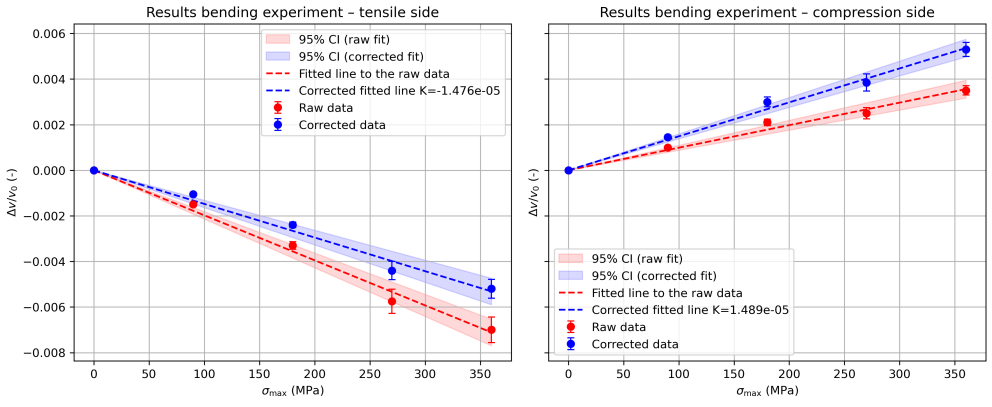
3.3. Results of the Bending Experiment

In the second experiment, the sample was tested in the bending platform, as described in Section 2.1.3. The measurement plan for this test is presented in Table 2. As observed, the applied force ranges from 300 to 1200 N, corresponding to stresses between 90 and 360 MPa at the specimen's bottom surface (in tension) and top surface (in compression), respectively. This force also results in deflections ranging from 0.61 to 2.44 mm.

Table 2. Measurement plan for the bending experiment.

Force [N]	Stress [MPa]	Deflection [mm]
300	90	0.61
600	180	1.22
900	270	1.83
1200	360	2.44

The results of the tensile stress measurements, when the sensors were positioned on the lower side, are plotted in Figure 13. As observed, there is a good linearly decreasing trend. The AEC is calculated as -14.75×10^{-6} MPa^{-1}, with a standard deviation of 7.615×10^{-7}.



(**a**) (**b**)

Figure 13. Results of the bending experiment. Velocity changes due to the applied bending stress for (**a**) tensile stress (specimen bottom surface) and (**b**) compressive stress (specimen top surface).

For the compressive stress case, the results shown in Figure 13 exhibit an upward trend, as expected. The resultant AEC for this experiment is 14.89×10^{-6} MPa^{-1}, with a standard deviation of 6.389×10^{-7}.

4. Discussion—Application to Long-Term Residual Stress Monitoring

The experiments reported in the previous sections have demonstrated an approximately linear correlation between the total stress in a specimen under tension or bending and the relative velocity change of the surface acoustic wave as induced and detected by inexpensive piezoelectric patch transducers. So far, this allows only the obvious conclusion from the velocity change to the *total* stress of a specimen or component. In the experiments reported here on thin strips, which may be assumed to be virtually free from (macroscopic) residual stresses, the total stress corresponds simply to the applied stress.

Our results further show that the acoustoelastic constant under uniaxial tension is slightly larger than under pure bending. This is physically consistent: in tension, the stress is essentially uniform over the penetration depth of the Rayleigh surface wave, whereas bending introduces pronounced stress gradients. Consequently, the effective stress sampled by the wave is reduced; moreover, depth-dependent material properties and the associated dispersion diminish the measured sensitivity, resulting in a smaller apparent constant in bending.

However, in general, the total stress in a component or structure is given by a superposition of applied load (primary) stress and residual (secondary) stress. Typically, components exposed to high-cycle fatigue loading are subjected to thermo-mechanical surface treatments prior to operation in order to generate compressive residual stresses, which have beneficial effects on component lifetime. However, the residual stresses may decay during long-time operation even under small cyclic loads. As component lifetime and inspection interval, respectively, depend markedly on the residual stress, this calls for the long-time residual stress monitoring, which is the subject of the present research.

During operation, SAW measurements always capture the superposition of applied (operational) and residual stresses; a direct separation is therefore not possible. Our approach relies on continuous monitoring and deliberately exploits naturally occurring idle (load-free) intervals. In these intervals, the applied stress vanishes, and the measured SAW response results solely from the residual-stress profile in the near-surface region. These reference points form the basis for the separation: by systematically comparing successive idle intervals, the temporal evolution of the residual stress—including possible relaxation—can be tracked directly. During loaded intervals, the SAW response reflects the sum of applied and residual contributions; by anchoring the residual level to the most recent reference value obtained in the nearest idle interval, the applied stress can be inferred as the deviation from this baseline—without additional load sensors.

Another approach is to make use of the load characteristics. Many components operate under conditions that do not change in the long term, i.e., the long-term average of the load stresses remains constant. Such a long-term average could span several days or weeks of operation. Now, if the residual stress remains constant, a running long-term average of the total stress, therefore, will also remain constant. Conversely, if the long-term average of the total stress changes, this means that the residual stress has changed by the same amount. For condition-based maintenance, it will in many cases suffice to track these long-term residual stress changes with respect to the initial (as-manufactured) state of the component.

The stress state in real components is far more complex than idealized loading cases. For parts containing residual stresses, a single measurement in one propagation direction is insufficient; instead, measurements along multiple directions are required to capture the orientation of the principal stresses. Direction-resolved measurements will allow the

reconstruction of wavefront distortion and thus the inference of principal stress directions and the multiaxial character of the stress state.

Stress gradients (e.g., due to bending or surface treatments) affect the propagation velocity, as it has been shown for the case of bending in the present work, and also cause dispersion.

Surface treatments (e.g., cold working or shot peening) additionally introduce significant plastic strains in the near-surface zone that shape the acoustoelastic response. If the material's flow curve is known, the measured velocity change can be used to infer the plastic strain and, in turn, the associated stresses. Physics-based, metal-mechanics models provide the link between microstructure, cold work, and the acoustoelastic effect [32].

5. Conclusions

This research introduced a novel system for continuous monitoring of stresses in metallic components relying on inexpensive sender and receiver piezoelectric patch transducers (PETs). The PETs generate and receive surface acoustic waves (SAWs), enabling estimation of the total stresses through the acoustoelastic effect.

To validate the stress estimation method, experiments were conducted using both a tensile stress test rig and a bending stress test rig under various applied stresses and excitation frequencies. The results demonstrate an approximately linear relation between stresses and relative velocity change of the acoustic waves, therefore allowing a straightforward estimation of the total stress from the wave velocity measurements. In many mechanical engineering applications, there exist idle times where no external load is present, and therefore the measured stress corresponds to the residual stress.

This offers, to the authors' best knowledge, for the first time a proof-of-principle of a method for inexpensive continuous non-destructive long-term monitoring of residual stresses applicable for condition-based maintenance. For the next step, long-term studies need to be conducted in order to assess the robustness and reliability of the proposed method.

Author Contributions: Conceptualization, M.R. (Mohsen Rezaei), S.E., and H.-P.G.; methodology, M.P., M.R. (Marcel Ruetz), M.R. (Mohsen Rezaei), and H.-P.G.; investigation, M.P. and M.R. (Marcel Ruetz); validation, M.R. (Mohsen Rezaei), S.E., and H.-P.G.; resources, S.E., J.M., and H.-P.G.; writing—original draft preparation, M.P., M.R. (Mohsen Rezaei), and M.R. (Marcel Ruetz); writing—review and editing, S.E., J.M., and H.-P.G.; supervision, M.R. (Mohsen Rezaei), S.E., and H.-P.G.; funding acquisition and project administration, J.M. and H.-P.G. All authors have read and agreed to the published version of the manuscript.

Funding: This research was funded by the Austrian Research Promotion Agency (FFG) within project FO999899048.

Institutional Review Board Statement: Not applicable.

Informed Consent Statement: Not applicable.

Data Availability Statement: There are no available public data.

Conflicts of Interest: Author Marcel Ruetz, Mohsen Rezaei, Maximilian Pfeiffer, Sven Eck, Jürgen Maierhofer and Hans-Peter Gänser are employed by the company Materials Center Leoben Forschung GmbH. The authors declare that the research was conducted in the absence of any commercial or financial relationships that could be construed as a potential conflict of interest.

Abbreviations

The following abbreviations are used in this manuscript:

AEC	Acoustoelastic coefficient
PET	Piezoelectric transducer
SAW	Surface acoustic waves
ToF	Time of flight
XRD	X-ray diffraction
ND	Neutron diffraction
MBN	Magnetic Barkhausen noise
BPF	Band-pass filter
LVM	Laser vibrometer

References

1. Hosford, W.F. *Mechanical Behavior of Materials*; Cambridge University Press: Cambridge, UK, 2005.
2. Withers, P.; Bhadeshia, H. Residual stress. Part 1—Measurement techniques. *Mater. Sci. Technol.* **2001**, *17*, 355–365. [CrossRef]
3. James, M.R. Relaxation of Residual Stresses an Overview. *Eng. Mater. Sci.* **1987**, *4*, 349–365.
4. Darmon, M. Special Issue on Ultrasonic Modeling for Non-Destructive Testing. *Appl. Sci.* **2024**, *14*, 2008. [CrossRef]
5. Guo, J.; Fu, H.; Pan, B.; Kang, R. Recent progress of residual stress measurement methods: A review. *Chin. J. Aeronaut.* **2021**, *34*, 54–78. [CrossRef]
6. Schajer, G.S. *Practical Residual Stress Measurement Methods*; John Wiley & Sons: Chichester, UK, 2013.
7. Noyan, I.C.; Cohen, J.B. *Residual Stress: Measurement by Diffraction and Interpretation*; Springer: New York, NY, USA, 1987. [CrossRef]
8. Birkett, A.J. The Use of Barkhausen Noise to Investigate Residual Stresses in Machined Components. In *Applied Stress Analysis*; Hyde, T.H., Ollerton, E., Eds.; Springer: Dordrecht, The Netherlands, 1990; pp. 72–81. [CrossRef]
9. Pitarresi, G.; Patterson, E. A review of the general theory of thermoelastic stress analysis. *J. Strain Anal. Eng. Des.* **2003**, *38*, 405–417. [CrossRef]
10. Andrés Zarate, E.; Custodio G, E.; Treviño-Palacios, C.G.; Rodríguez-Vera, R.; Puga-Soberanes, H.J. Defect detection in metals using electronic speckle pattern interferometry. *Sol. Energy Mater. Sol. Cells* **2005**, *88*, 217–225. [CrossRef]
11. Gu, B.; Wang, Y.; Gao, L.; Xu, G.; Liu, L.; Sun, S. Effects of ultrasonic impact treatment on the tensile properties of DH36 steel welded joints. *Eng. Fract. Mech.* **2025**, *315*, 110798. [CrossRef]
12. Lu, Y.; Dong, J.; Li, W.; Wang, C.; Shen, R.; Jiang, D.; Yi, Y.; Wu, B.; Sun, G.; Zhang, Y. Online Characterization of Internal Stress in Aluminum Alloys During Laser-Directed Energy Deposition. *Sensors* **2025**, *25*, 2584. [CrossRef] [PubMed]
13. Hughes, D.S.; Kelly, J.L. Second-Order Elastic Deformation of Solids. *Phys. Rev.* **1953**, *92*, 1145–1149. [CrossRef]
14. Murnaghan, F.D. Finite Deformations of an Elastic Solid. *Am. J. Math.* **1937**, *59*, 235–260. [CrossRef]
15. Toupin, R.A.; Bernstein, B. Sound Waves in Deformed Perfectly Elastic Materials. Acoustoelastic Effect. *J. Acoust. Soc. Am.* **1961**, *33*, 216–225. [CrossRef]
16. Hayes, M.; Rivlin, R.S. Propagation of a plane wave in an isotropic elastic material subjected to pure homogeneous deformation. *Arch. Ration. Mech. Anal.* **1961**, *8*, 15–22. [CrossRef]
17. Crecraft, D. The measurement of applied and residual stresses in metals using ultrasonic waves. *J. Sound Vib.* **1967**, *5*, 173–192. [CrossRef]
18. Zhong, B.; Zhu, J.; Morcous, G. Measuring acoustoelastic coefficients for stress evaluation in concrete. *Constr. Build. Mater.* **2021**, *309*, 125127. [CrossRef]
19. Hwang, Y.I.; Kim, G.; Kim, Y.I.; Park, J.H.; Choi, M.Y.; Kim, K.B. Experimental Measurement of Residual Stress Distribution in Rail Specimens Using Ultrasonic LCR Waves. *Appl. Sci.* **2021**, *11*, 9306. [CrossRef]
20. Zernov, V.; Fradkin, L.; Gautesen, A.; Darmon, M.; Calmon, P. Wedge diffraction of a critically incident Gaussian beam. *Wave Motion* **2013**, *50*, 708–722. [CrossRef]
21. Fradkin, L.; Darmon, M.; Chatillon, S.; Calmon, P. A semi-numerical model for near-critical angle. *J. Acoust. Soc. Am.* **2013**, *139*, 141–150. [CrossRef]
22. Garcia Ruano, S.; Delijaicov, S.; dos Santos Junior, A. Acoustoelasticity to measure residual stresses in plates of 5052 aluminum joined by FSW. *J. Braz. Soc. Mech. Sci. Eng.* **2023**, *45*, 82. [CrossRef]
23. Xu, M.; Zhao, H.; Liu, C.; Zhan, Y. A new approach for the inversion of residual stress based on acoustoelasticity theory and full waveform inversion. *arXiv* **2025**, arXiv:2410.10067. [CrossRef]

24. PI Ceramic. P-876 DuraAct Patch Transducer. Available online: https://www.piceramic.com/en/products/piezoceramic-actuators/patch-transducers/p-876-duraact-patch-transducer-101790 (accessed on 13 February 2025).
25. Capineri, L.; Bulletti, A. Ultrasonic Guided-Waves Sensors and Integrated Structural Health Monitoring Systems for Impact Detection and Localization: A Review. *Sensors* **2021**, *21*, 2929. [CrossRef]
26. Rezaei, M.; Eck, S.; Fichtenbauer, S.; Maierhofer, J.; Klambauer, R.; Bergmann, A.; Künstner, D.; Velic, D.; Gänser, H.P. Real-Time Detection and Quantification of Rail Surface Cracks Using Surface Acoustic Waves and Piezoelectric Patch Transducers. *Sensors* **2025**, *25*, 3014. [CrossRef] [PubMed]
27. GAMPT mbH. CW Generator SC600. Available online: https://www.gampt.de/en/product/cw-generator-sc600/ (accessed on 13 February 2025).
28. PicoScope 5000 Series Flexible Resolution Oscilloscopes. Available online: https://www.picotech.com/oscilloscope/5000/flexible-resolution-oscilloscope (accessed on 13 February 2025).
29. Knapp, C.H.; Carter, G.C. Generalized Correlation Method for Estimation of Time Delay. *IEEE Trans. Acoust. Speech Signal Process.* **1975**, *24*, 320–327. [CrossRef]
30. Wang, S.; Li, Z.; Wang, P.; Chen, H. Optimization Algorithm for Delay Estimation Based on Singular Value Decomposition and Improved GCC-PHAT Weighting. *Sensors* **2022**, *22*, 7254. [CrossRef]
31. Liu, W.; Li, M.; Wang, T.; Jin, M.; Fang, Q. Research on Time Delay Estimation Method of Partial Discharges Signal with Improved Weighted Function. *Electronics* **2023**, *12*, 4196. [CrossRef]
32. Ruetz, M.; Antretter, T.; Gänser, H.P. Metal physics based model for predicting the influence of plastic cold-working on the acoustoelastic effect. *Comput. Mater. Sci.* **2025**, *259*, 114123. [CrossRef]

Disclaimer/Publisher's Note: The statements, opinions and data contained in all publications are solely those of the individual author(s) and contributor(s) and not of MDPI and/or the editor(s). MDPI and/or the editor(s) disclaim responsibility for any injury to people or property resulting from any ideas, methods, instructions or products referred to in the content.